

METHODS

Hydrographic Regimes

We conducted a review and synthesis of hydrologic data of the Upper Snake River that was published as a technical report to the Reclamation, Boise, Idaho. This report titled: “Review and Synthesis of Riverine Databases and Ecological Studies in the Upper Snake River, Idaho” (Hauer et al 2002), provides important background data and analysis used in the interpretation of the data presented herein. We refer the reader to that report; however, we have included essential duplicative data here. We have also conducted additional analyses that are specific to the questions addressed in this report and play a significant role in the interpretations and recommendations appearing below.

The discharge data presented throughout this report are based on the daily discharge records obtained from the United States Geological Survey stream flow database for Idaho, <http://id.water.usgs.gov/> and Wyoming, <http://wy-water.usgs.gov/>.

Temperature and Groundwater-Surface Water Interactions

Temperature data were obtained in selected regions of the Fisher floodplain to examine thermal variation and its distribution across unconfined river reaches that showed strong affinities for groundwater – surface water interactions. Temperature loggers were placed in hydrogeomorphic locations showing groundwater return to selected off-channel aquatic habitats. Loggers were placed in the study habitats and secured with iron rebar and plastic coated wire. Each logger collected temperature data °C at 2hr intervals from mid-August 2001 to mid November 2002.

Groundwater – surface water interactions on the Fisher floodplain were documented by placing piezometers into the floodplain substratum at various locations along the river gradient of the floodplain. Piezometers were installed using the methods described in Baxter et al. (2003) and were analyzed for vertical hydraulic gradient (VHG) which as a correlative measure of the piezometric surface and position of “upwelling” (+VHG) and “downwelling” (-VHG) zones on the floodplain.

Remotely Sensed Hyperspectral Data

Airborne remotely sensed data were collected with an AISA hyperspectral imagery system from Spectral Imaging, Oulu, Finland. The AISA system consists of a compact hyperspectral sensor head, miniature GPS/INS sensor, and system control and data acquisition unit. The AISA hyperspectral sensor is operated from the aircraft at the height (1000m) and speed (87kts) required to generate a 1x1m pixel resolution. Waveband configuration for digital data acquisition is from 256 individual spectral wavebands (400 to 950 nm) arrayed into 20 aggregate bands. The system also requires an aircraft top-mount of a real-time fiber-optic downwelling irradiance sensor (FODIS) that provides radiometric correction data for post-processing of surface reflectance. The GPS/INS is a Systron-Donner C-MIGITS III with Digital Quartz Inertial measurement unit (DQI) which tags each image line from the AISA sensor. The GPS coordinates are derived from 10 to 12 GPS satellites depending on satellite positions. The GPS data are linked with the inertial referencing of the C-MIGITS III to correct for pitch, roll and yaw of the aircraft during data acquisition. Data are stored during acquisition on a hot-swap removable U160 SCSI drive.

The remote sensing data were collected along predetermined flight lines oriented along the long axis of the study floodplains and having flight line overlaps of 40-50%. All data were collected within a time period of 1.5 hrs either side of solar noon. We selected the clearest days possible during a sampling interval spanning several weeks to capture flow and vegetation attributes that were targeted for the particular season and to maximize the quality of the imagery data.

Individual flight lines were cross-referenced with existing Digital Ortho Photo Quadrangles (DOQs) to examine the spatial positioning of each flight line. If an individual flight line needed further geo-rectification, then additional GCPs (ground control points) were added to improve the rectification in a given flight line. All geo-rectified flight lines had a mean RMS (root mean square) error of less than 4 meters (Table 1). The RMS error is an estimate of how close a given pixel is to its true location. Once all flight lines were geo-rectified for a given reach they were then stitched together to create a final mosaic. Minor color-balancing between flight lines were applied during the mosaiking process. All geo-rectification and mosaiking were completed in Erdas Imagine 8.5.

In addition to rectification errors, rapid turbulence experienced during data acquisition occasionally caused the aircraft to roll at a rate faster than the GPS/IMU data stream. Turbulence Induced Error (TIE) during image acquisition resulted in image distortion for some areas. These distortions were highly localized and appear as waves in the imagery. Rectification errors as well as errors caused by aircraft turbulence affect accuracy assessments causing portions of the image to be spatially offset from the true location. Rectification errors are inherent in virtually all remotely sensed data. The rectification errors we encountered represent variation generally less than 5% for all reaches.

Table 1. Mean RMS errors generated for each reach. The RMS error provides an estimate of how far off a given pixel is from its true location.

Mean RMS error	
Swan	3.3
Conant	3.8
Fisher	3.3
Heise	3
Twin	2.8

Water Depth and Velocity Ground-truth

A Sontek RS3000 Acoustic Doppler velocity-Profiler (ADP) was used to acquire detailed water depth and vertical profile measurements of flow velocity along channel reaches within the study floodplains. The ADP uses 3 transducers to generate a 3 MHz sound pulse into the water. As the sound travels through the water, it is reflected in all directions by particulate matter (e.g., sediment, biological matter) carried with the flow. The sonar signal is most strongly reflected from the bottom substrate providing a measure of water depth. Some portion of the reflected energy travels back toward the transducer where the processing electronics measure the change in frequency as a Doppler shift. The Doppler shift is correlated to the velocity of the water. The ADP operates using three transducers generating beams with different orientations relative to the flow of water. The velocity measured by each ADP transducer is along the axis of its acoustic beam. These beam velocities are converted to XYZ (Cartesian) velocities using the relative orientation of the acoustic beams, giving a 3-D velocity field relative to the orientation of the ADP. Since it is not always possible to control instrument orientation, the ADP includes an internal compass and tilt sensor to report 3-D velocity data in Earth (East-North-Up or ENU) coordinates, independent of instrument orientation. Hence, it is possible to determine the mean flow velocity in separate cells through the water column oriented perpendicular to the flow field.

By measuring the return signal at different times following the transmit pulse, the ADP measures water velocity at different distances from the transducer beginning just below the water surface and continuing to the bottom. The water velocity profile is measured and displayed as a series of separate 15 cm deep cells from top to bottom. Each recorded cell measurement is the average of several hundred measures over a 5 second time intervals.

We deployed the ADP from the front of a small jet-boat with both velocity profile data and depth data correlated spatially by linking a GPS (Global Positioning System) receiver co-located with the position of the ADP (Figure 5). During data acquisition the ADP was maneuvered back and forth across the channel to obtain data from as full an array of aquatic habitats, depths and velocities as possible. Both the ADP and GPS data were recorded simultaneously on a field laptop computer. The ADP data were then processed to create an integrated velocity value (average velocity for an individual ADP profile), as well as a depth value for each GPS location.

Four ADP surveys were collected in summer and fall of 2002 for each floodplain reach (June 20-22, August 17-20, September 24–26, November 25-26). The Heise reach was excluded from the November ADP survey due to technical difficulties with the ADP. The ADP data were obtained for base flow discharge at 1,500 cfs, and at discharges of 5,000, 8,000 and 11,500 cfs (Figure 6). Over 25,000 discrete measures of depth and flow velocity were recorded during the ADP surveys (Table 2).

Initial Depth and Velocity Classification

The integrated velocity and depth data from the ADP were combined with the September hyperspectral data for all reaches in a GIS to classify the variance in spectral reflectance of water

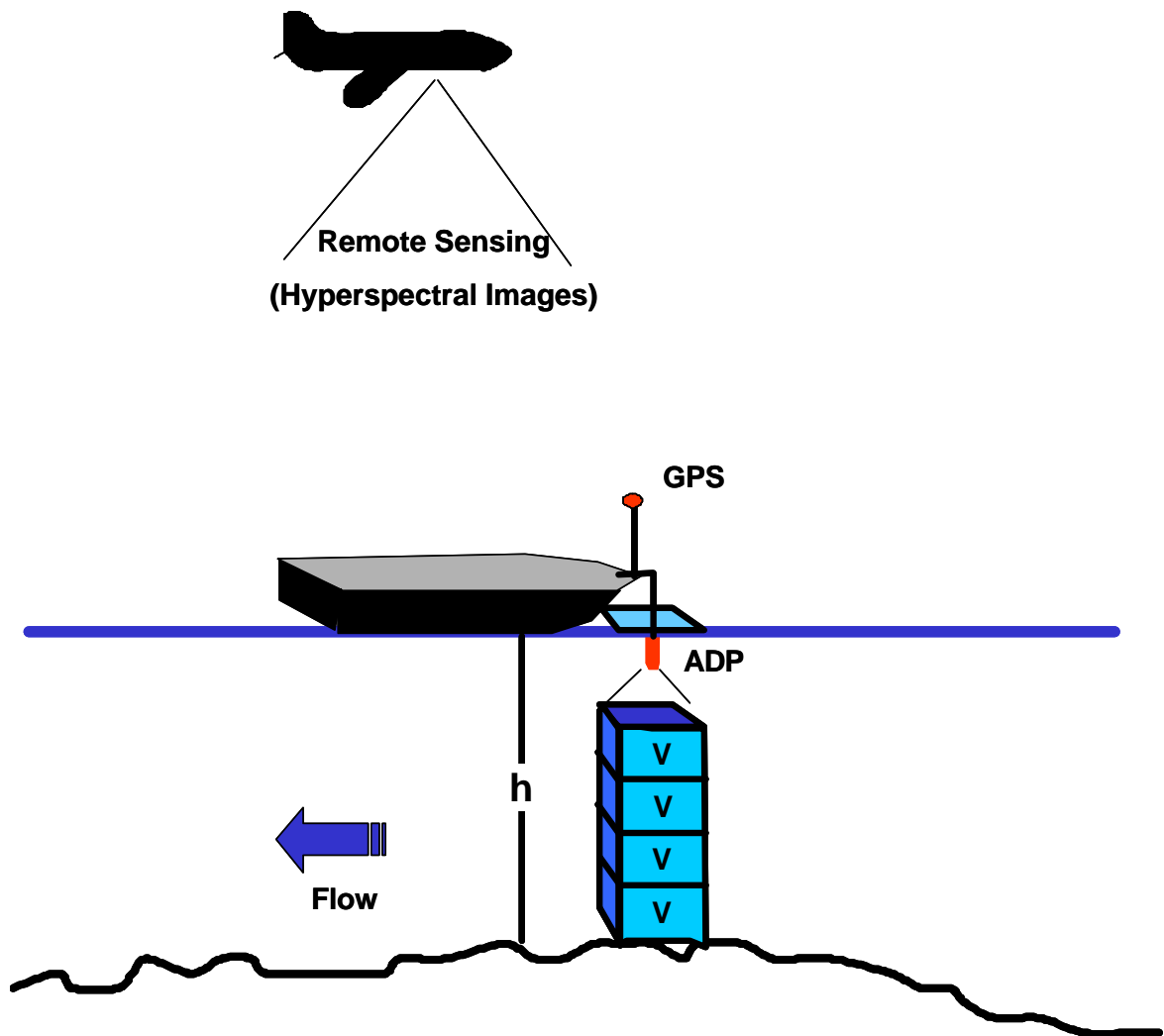


Figure 5. Illustration of linkage between remotely sensed hyperspectral data, which is geospatially explicit and the field data collection of depth (h) and velocity (V) using a boat mounted **A**coustic **D**oppler **V**elocity **P**rofiler (ADP) in conjunction with a Global Positioning System (GPS). All ADP data were GPS tagged to relate directly with the hyperspectral data.

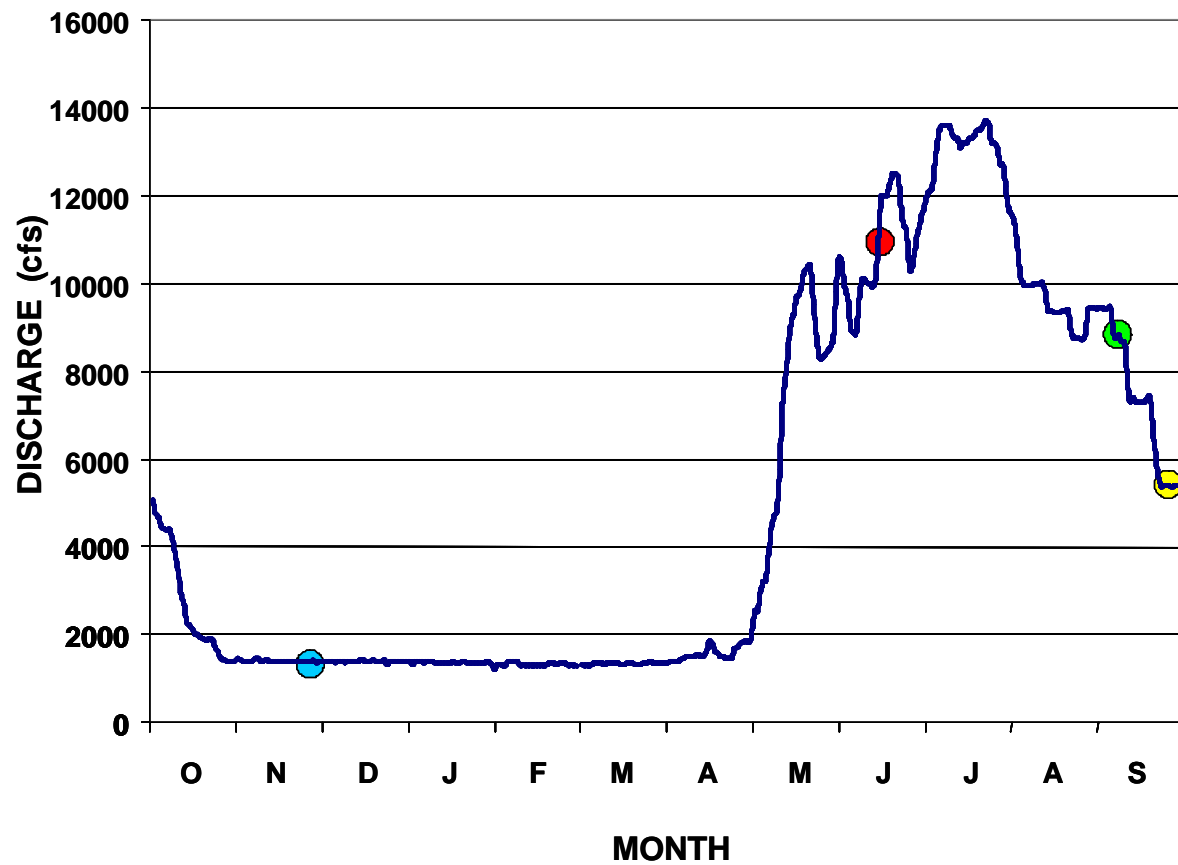


Figure 6. Annual hydrograph of Water Year 2002 illustrating the discharge and times of the year that ADP data were collected from the study floodplains of the Snake River .

Table 2. Total number of measures taken with the ADP of water depth and integrated flow velocities for each sample date shown in Figure 6.

Date	Total number of profiles
June 20 -22	8,654
August 17- 20	9,449
September 24 - 26	5,571
November 25-26	1,434
	25,108

depth and flow velocity. An unsupervised classification approach (ISODATA, Iterative Self-Ordering Data Analysis, Tou and Gonzalez 1977) was used to generate similar categories of spectral reflectance (Figure 7). Once an unsupervised classification of spectral reflectance was generated, the ADP data were distributed in the GIS environment to aggregate classes and assign unique depth and velocity categories. All reaches were classified into five depth categories (<0.5 , $0.5 - 1$, $1 - 1.5$, $1.5 - 2.0$, and > 2.0 m) and five velocity categories (< 0.5 , $0.5 - 1.0$, $1.0 - 1.5$, $1.5 - 2$, and > 2.0 m/s). These initial classifications of water depth and flow velocity (Figure 8) provided the basis for modeling depths and velocities at both higher and lower river stages. The ranges for each category were a function of the range of depths and flow velocity obtained with the ADP and the resolution that can be achieved from the hyperspectral imagery.

Two methods were used to assess the accuracy of the depth and velocity classifications. Traditionally, the accuracy of a classification is assessed by comparing the reference data (e.g., ADP survey data) with values on the classification map. This method is generally referred to as the ‘pure’ accuracy assessment. However, in spatial representations of continuous data (e.g., depth and velocity data) where sharp boundaries between classes rarely occur, it is preferable to apply a ‘fuzzy’ assessment of classification accuracy (Gopal and Woodcock 1994, Muller et al. 1998). The ‘fuzzy’ assessment allows determination of variance within the reference data and its departure from that classified in adjacent classes (i.e., one class above or one class below the depth or velocity classification being tested). Error matrices were generated for each floodplain, and include both the ‘pure’ and ‘fuzzy’ assessments (Table 3).

Some of the error between measured and classified depths and velocities are undoubtedly related to the rectification errors and the distortions discussed above caused by TIE, as well as error associated with the relative accuracy of the GPS. The accuracy of real time GPS data

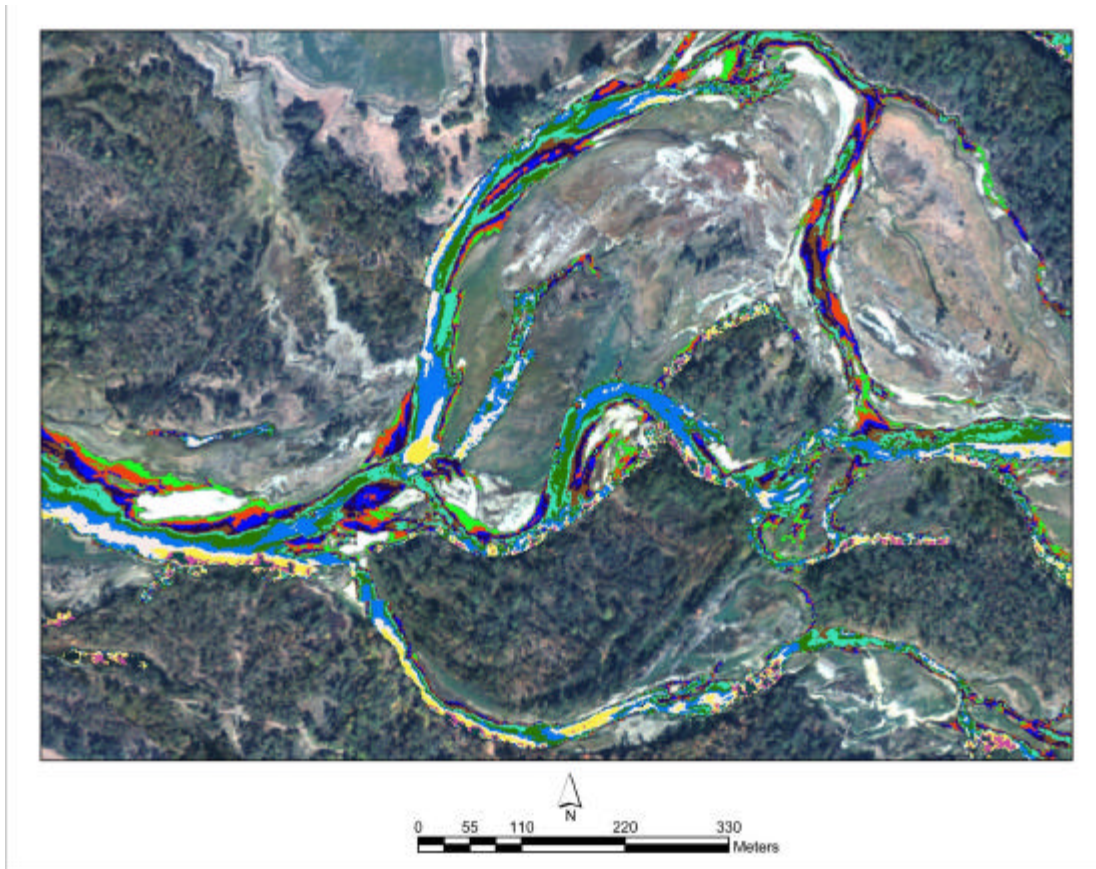


Figure 7. Unsupervised classification of hyperspectral data extracting spectral reflectance characteristics of water. These data illustrate the variation in spectral reflectance used to classify hydraulic characteristics.

Table 3. Accuracy assessment for all reaches at 5000 cfs; summarized as pure and fuzzy percentages.

	Depth		Velocity	
Flood Plain	Pure(%)	Fuzzy(%)	Pure(%)	Fuzzy(%)
Swan	60	97	33	74
Conant	53	89	43	85
Fisher	61	91	62	88
Heise	72	94	52	90
Twin	47	86	50	87

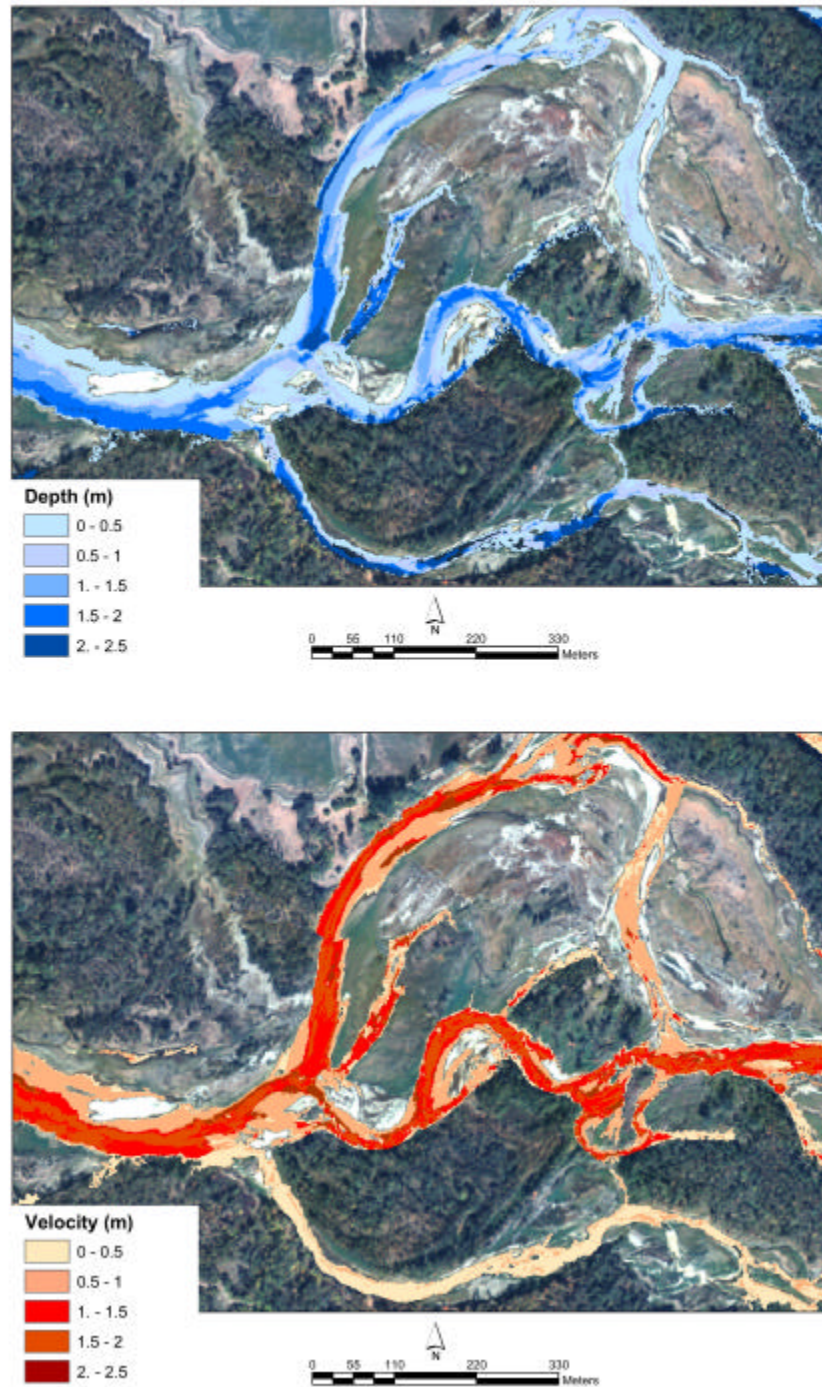


Figure 8. ADP data were distributed in the GIS environment to aggregate classes and assign unique depth and velocity categories. These initial classifications of water depth and flow velocity, illustrated here, form the basis of the following hydraulic and habitat classifications.

varies as a function of the number of satellites available and their position in the sky. In addition, both velocity and depth are recorded as the average velocity over a 5 second interval. Thus, depending on flow and geomorphic conditions, an individual profile could be an average of multiple flow and depth conditions for a given GPS location. Hence, the true ADP position can be as much as 3 to 4 m away from the GPS recorded position resulting in variance between the measured ADP profile and the hyperspectral imagery.

Rectification errors, aircraft turbulence distortions, and GPS errors (Figure 9) all contribute to potential misclassifications in the accuracy assessments. These errors account for 5 to 15% of the error in the 'pure' accuracy assessment. However, the use of the 'fuzzy' assessment helps minimize these affects, by evaluating classification within the context of neighboring classes. While the 'fuzzy' assessment may overestimate the classification accuracy, the 'pure' assessment clearly underestimates the accuracy. Despite the various sources of potential error, hydrologic and geomorphic structure (i.e., depth and velocity) and the associated aquatic habitats (i.e., pools, riffles, rapids and shallows) all appear in appropriate juxtapositions and orientations in river channels and distributed across the floodplain in logical places that we were able to confirm through direct observation in the field.

Creating a Floodplain Digital Elevation Model (DEM)

We produced a detailed floodplain DEM from the hyperspectral imagery and ground based topographic surveys. We then used the discharge stage level on the dates of the remote sensing image acquisitions to establish elevation reference from which to evaluate water depth across all discharges. This allowed delineation of floodplain areas likely to be inundated and reworked during potential flooding events.

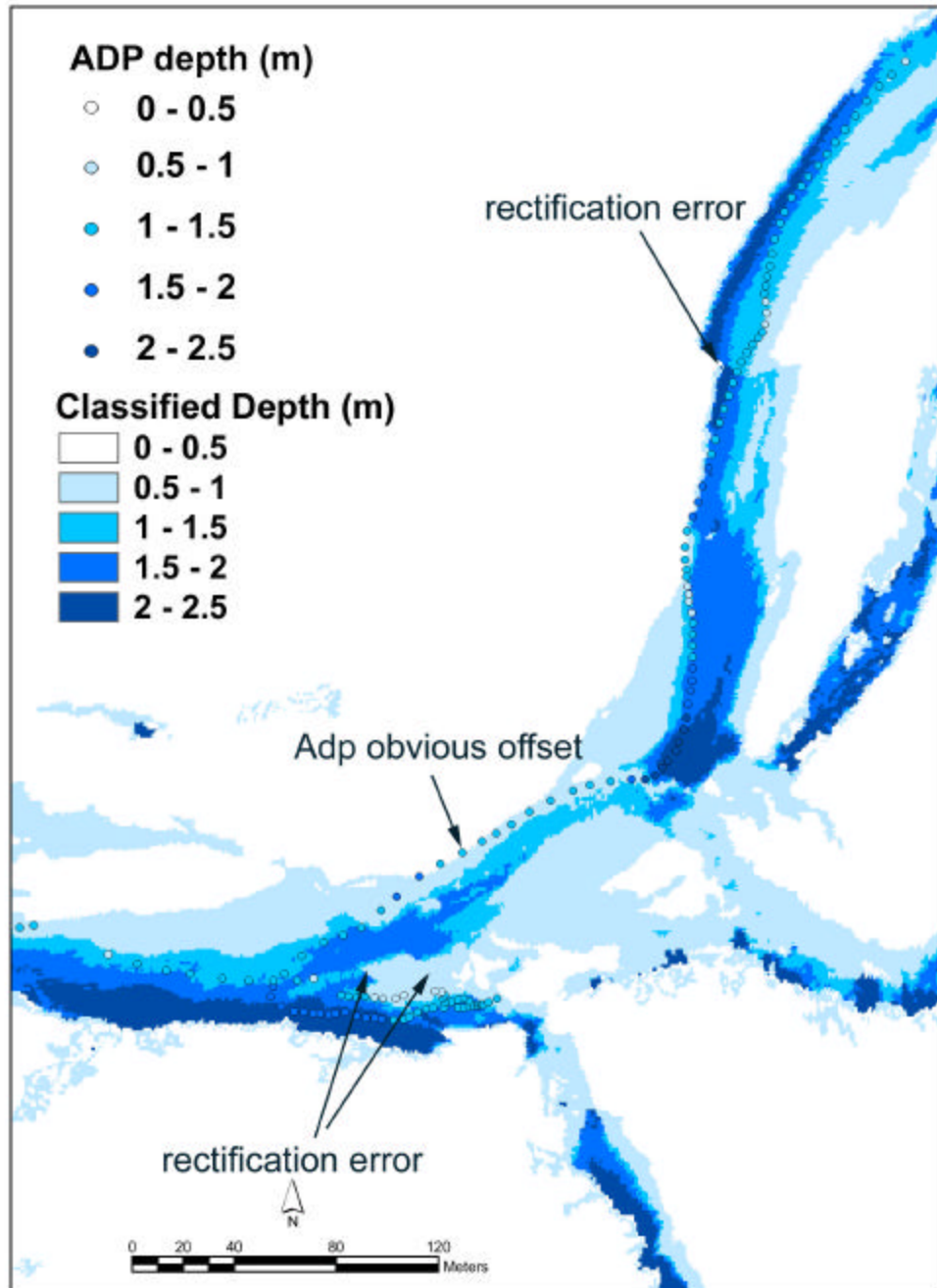


Figure 9. Typical rectification errors and misalignment of ADP tracks caused by inherent GPS error, georectification error and turbulence during hyperspectral data collection.

One-meter contour intervals were derived by re-sampling the 30 m resolution USGS DEM information. These data were superimposed onto the co-registered, hyperspectral imagery to provide first-order estimates of floodplain slopes. However, this level of topographic information was not of sufficient resolution to delineate detailed floodplain topography, especially critical features such as relic backwater channels that may provide new channels following future avulsions. Moreover, it is not feasible to use traditional survey methods to measure the topography adequately over the many square kilometers represented by our floodplain study reaches. To obtain sufficient topographic information for our modeling needs, we combined focused topographical survey information with airborne remote sensing data to assign relative elevations to classified floodplain cover type features (Figure 10).

Topographic surveys were conducted along transects that extended across the floodplain. These transects were chosen to include a broad range of topography (e.g., slope, elevation) across as many cover type features as possible. Other features captured by these surveys included relative elevations and slopes between gravel bars, water surface and bank top elevations throughout the floodplain reach. Unsupervised and supervised classifications of the airborne hyperspectral remote sensing imagery were conducted to classify major land cover features, including vegetation (e.g., grassland, forest), side channels, springbrooks, cobble bars, terraces and others. The survey data was then overlaid on the various classified cover types and assigned a relative elevation to the main channel, as well as a typical slope value, to characterize the transition from one cover type to the next. For example, water surface elevation in the main channel was set to zero in all cross-sections and all other cover types were assigned relative elevations (i.e., +/- change in elevation from the main channel). Hence, relative elevations and slopes, both across and between cover types, were assigned to the identified major land cover

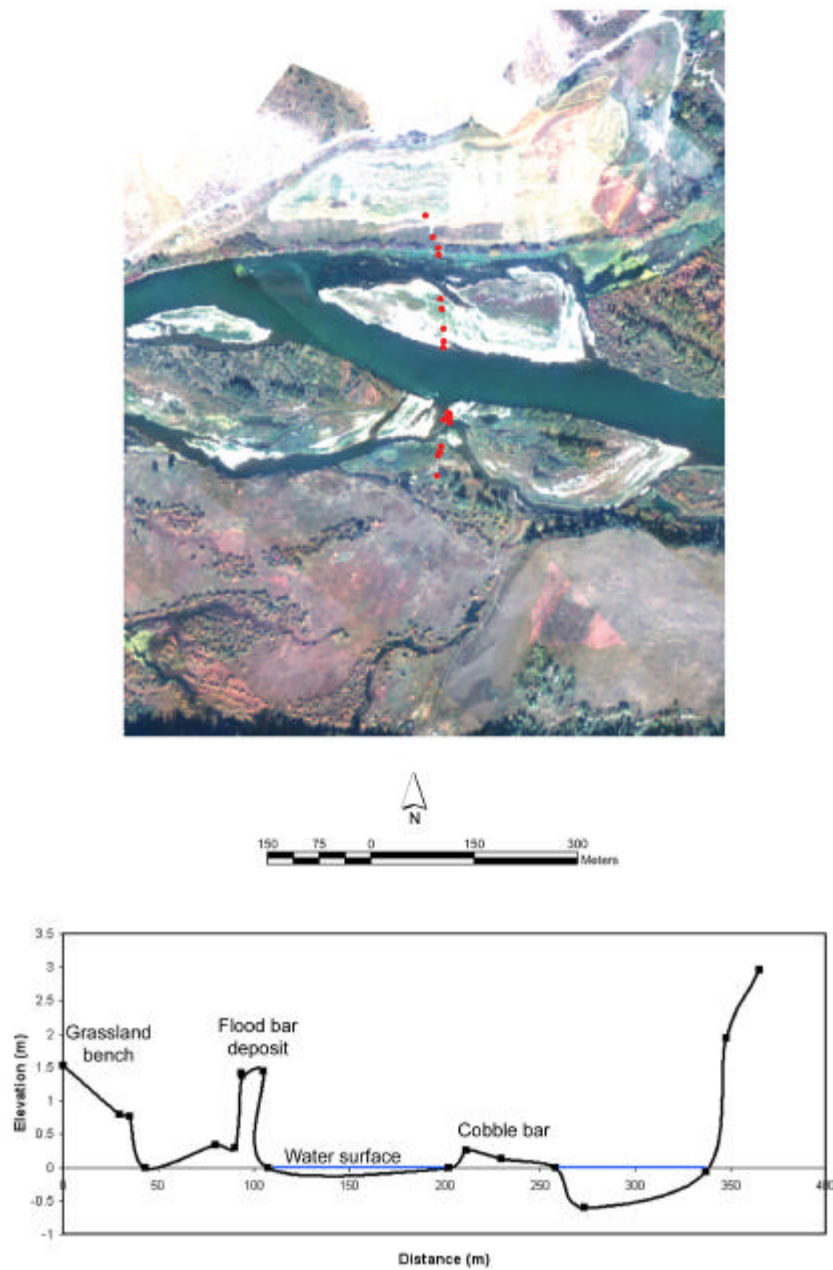


Figure 10. Survey data points are represented by red dots in the hyperspectral image of the Fisher floodplain (top panel). A cross-sectional plot of the survey data is shown in the lower panel.

features classified from the hyperspectral imagery. With this combination of data (i.e., survey data, hyperspectral imagery, and the USGS DEM) we were able to produce a high resolution DEM of each floodplain.

Floodplain inundation was modeled at 10cm stage increments using the higher resolution DEM. We compared modeled flood inundation, with geo-rectified imagery on June 20, 2002 (~11,000 cfs) and April 12, 2003 (~1500 cfs) to match discharge with inundation extent for each reach. Similarly, we used airborne video taken on June 17, 1997 (~37000 cfs) to generate flood inundation maps for each reach. These three inundation maps (Figure 11) were used to calibrate our stage-discharge relationships for each reach.

Modeling Flow Depth and Velocity at Higher Discharges

We modeled flow velocity at varying discharges by establishing a basic relationship between velocity and river stage for all reaches. This relationship was developed by multiple measures of flow and depth at various discharge levels during the duration of our study (discussed above). Our modeling algorithms also included flow velocities for areas of the floodplain where flow velocity decreases as stage increases due to incorporation of large flow resistance elements. However, we were not able to accurately predict the formation or existence of slow or even calm “eddy drop zones” that occur on the shorelines bordering the downstream end of a riffle or rapid that dumps into a run. Fortunately, these water types do not represent a large portion of the total water surface area being modeled nor are they important for estimating avulsion processes. Although we were not able to directly model eddy drop zones in association with riffles and rapids, which are important potential aquatic habitats, we can accurately model

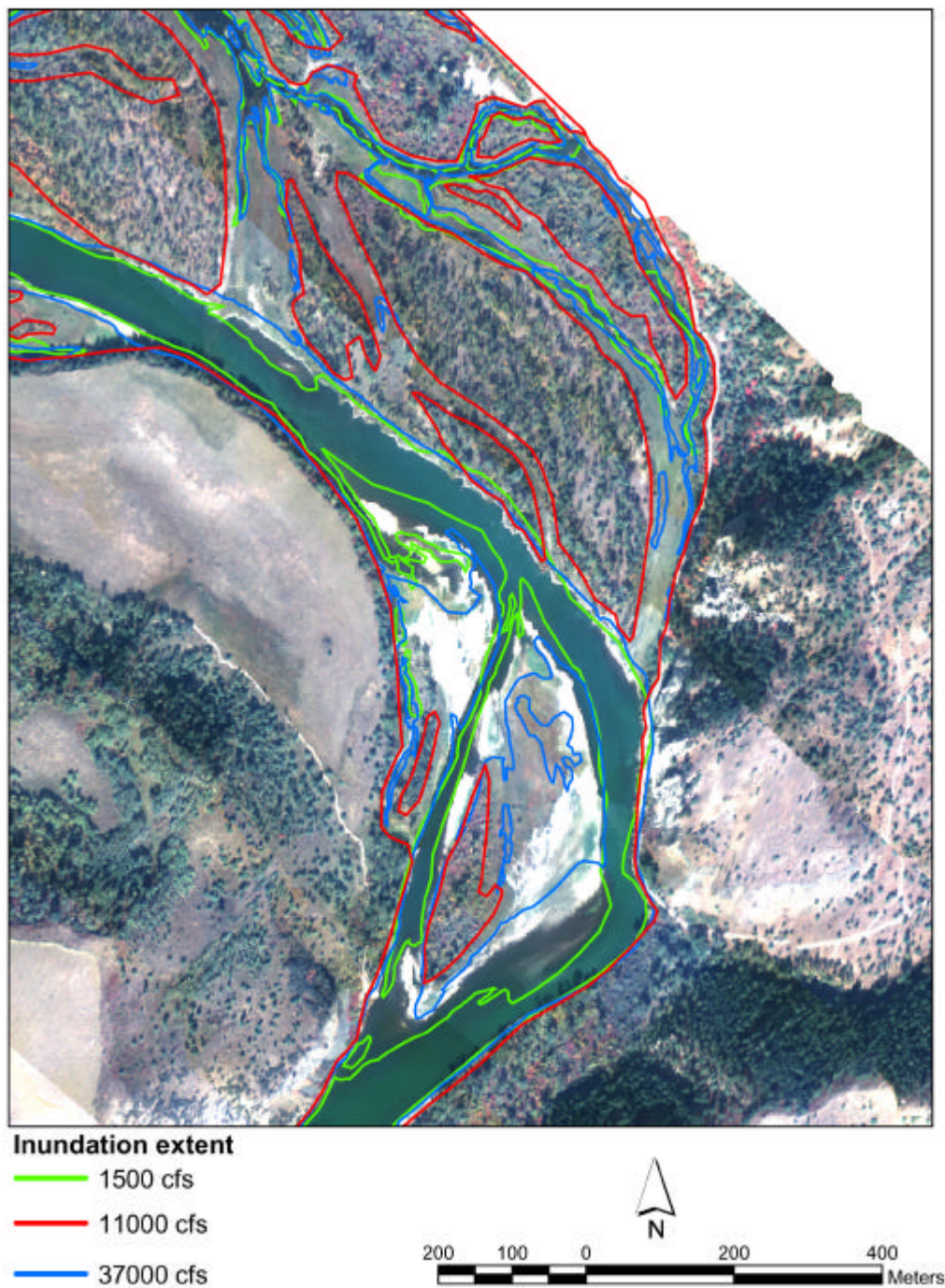


Figure 11. Colored lines show the extent of inundation for three different levels of discharge on this hyperspectral image of a portion of the Fisher floodplain.

changes in the associated water types (e.g. riffles, rapids and runs) and identify ecotones characterized by rapid change in velocity (see discussion of aquatic habitat below).

Estimates of flow velocity for the flooding scenarios were based on the initial velocity classification generated from the September imagery (5,000 cfs). Velocity was then increased according to equations (1) and (2) below, generated from depth-velocity relationships measured in the ADP surveys (Figure 12) and the data collected from a hand-held ADV (Acoustic Doppler Velocimeter) (Figure 13). The hand-held ADV was used exclusively in shallow waters (< 1 m) where the boat-mounted ADP loses signal. Equation 1 was used to simulate velocity for water depths > 0.8 m and equation 2 was used for water depths < 0.8 m, where x is the water depth at a given stage.

$$y = 0.4493 \ln(x) + 1.3986 \quad (1)$$

$$y = 1.789(x) - 0.2042 \quad (2)$$

After velocity was modeled for a given stage, we set an upper limit on water velocity for each modeled depth based on a Froude threshold (Figure 14). Using 10 cm stage increments, depths and velocities were modeled for each reach to represent discharge regimes from 1,500 cfs to 37,000 cfs. To check the accuracy of the modeled velocities and depths, the ADP surveys from November (1,500 cfs), August (8,000 cfs), and June (11,000 cfs) were used as reference data. For example, from the stage-discharge relationships in the Conant reach, we estimated the 11,000 cfs discharge corresponded to a stage increase of 0.5 m. Using the depths and velocities that were modeled at the 0.5 m stage increase, error matrices (Table 6) were generated from the appropriate ADP survey (i.e., the 11000 cfs survey) to validate the modeled results of depth and velocity (Figure 15). Our modeled estimates of flow velocity are in the same range

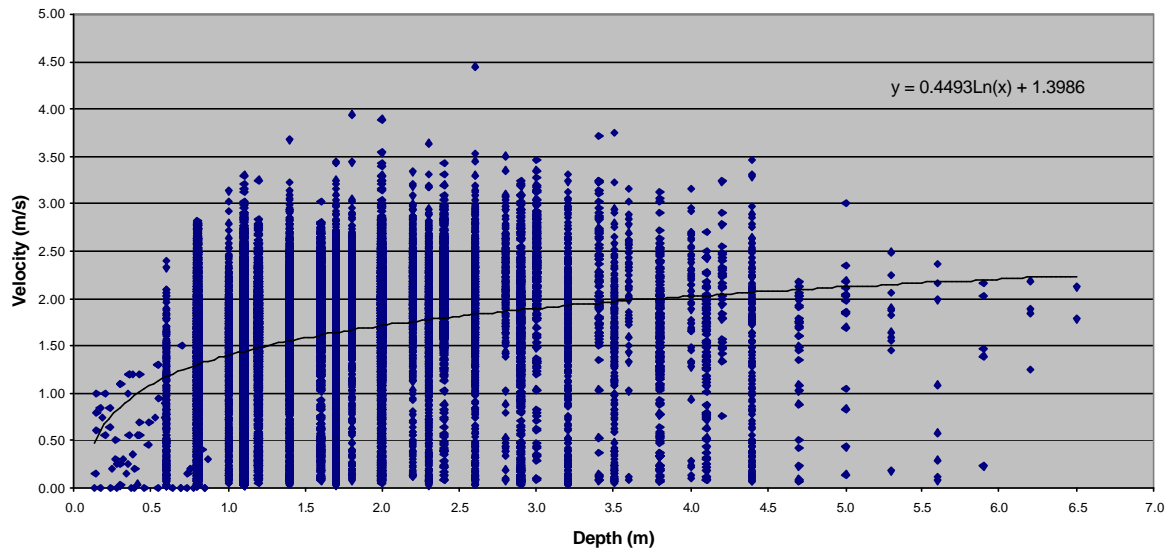


Figure 12. A plot of measured water depth and flow velocity for 25,308, locations from all floodplains in the study over 5 discharge levels. The log regression curve of these data was used to determine variation in flow velocity with change in stage.

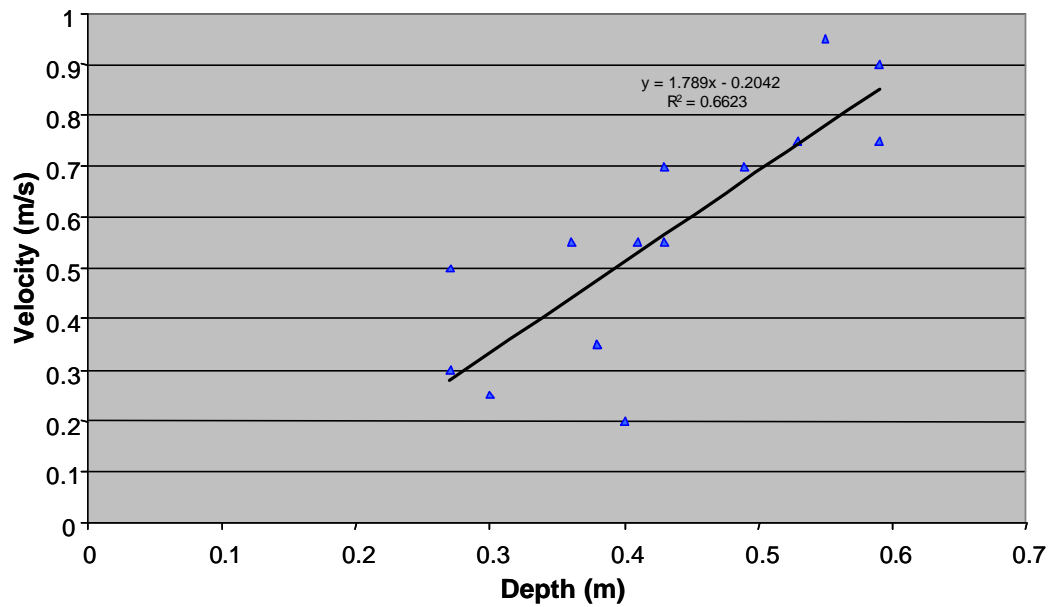


Figure 13. Correlation between measured water depth and flow velocity for water depths < 0.8 m across in a single shallow riffle area.

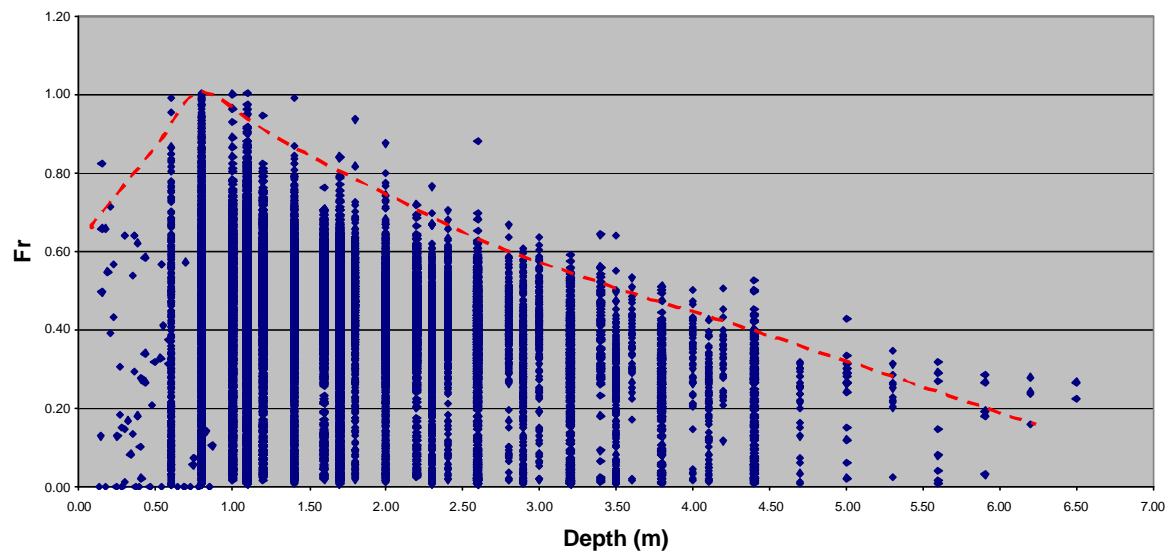


Figure 14. A plot of Froude number vs water depth for all ADP measures. The red line represents the accepted Froude maximum used in the GIS modeling of flow velocities.

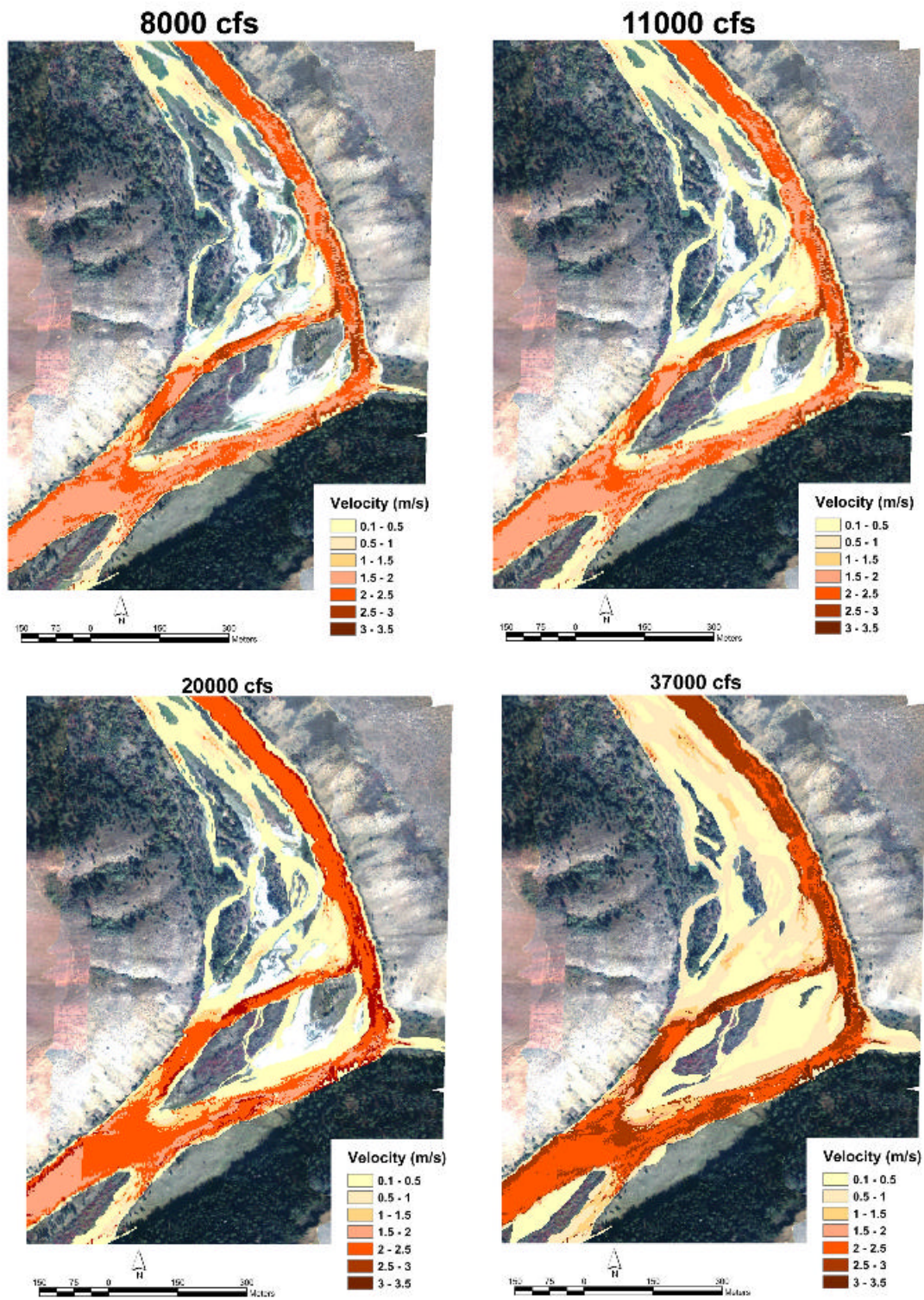


Figure 15. A plot of the spatial distribution of modeled flow velocity for discharges of 8000 11000, 20000, and 37000 cfs in the lower part of the Conant floodplain.

of accuracy we found for the original classification of the hyperspectral imagery at 5,000 cfs (Table 4). However, we are much better at estimating flood velocities versus flow velocity for base flows. This is probably due to the difference between local energy gradients increasing as stage drops making it difficult to accurately model a change in velocity based on a linear equation.

Aquatic Habitats

Aquatic habitats were derived from a combination of depth and velocity classification data, modeling output, and known relative positions of habitats associated with different channel and floodplain characteristics. As 1x1m unique classifications, pixels of one classification may appear within a group of pixels classified to a different depth and velocity. This often gives the appearance of stippling in the classified image. In our habitat classification procedure, we first aggregated depth-velocity pixels (DVP) into common patches, plotted as polygons, by conducting a “majority filter” step in the GIS environment. Each filtered DVP patch was then assigned a unique aquatic habitat type. The area and dimensions for each aquatic habitat across each of 5 discharges (1500, 5000, 11600, 25000, 37000 cfs) was then compiled through the GIS. We then analyzed the various characteristics of the aquatic habitat patches (e.g., patch shape, edge relationship, edge length).

Vegetation classification

The September imagery was used for land cover classification because of the high contrast between vegetation types during autumnal senescence. A combination of supervised and unsupervised classifications was used to produce a land cover map for each reach. First, an

Table 4. An example of error assessment tables for each class of depth and velocity for the Conant Valley flood plain at 11,000 cfs.

Conant Velocity 11000 cfs

Classified (m/s)	Reference (m/s)					Classified Total	User's Accuracy Pure (% correct)	User's Accuracy Fuzzy (% correct)
	0 - 0.5	0.5 - 1	1 - 1.5	1.5 - 2	> 2			
0 - 0.5	9		4			13	69.23	69.23
0.5 - 1		1	3	3	1	8	12.50	50.00
1 - 1.5	2	6	5	6	2	21	23.81	80.95
1.5 - 2		2	33	95	167	297	31.99	99.33
> 2		6	18	59	164	247	66.40	90.28
Reference Total	11	15	63	163	334	586	0.46757679 548 0.93515358	
Producer's Accuracy Pure (% correct)	81.82	6.67	7.94	58.28	49.10			
Producer's Accuracy Fuzzy (% correct)	81.82	46.67	65.08	98.16	99.10			
Overall Classification Pure = 46.76%								
Overall Classification Fuzzy = 93.52%								

Conant Depth 11000 cfs

Classified (m)	Reference (m)				Classified Total	User's Accuracy Pure (% correct)	User's Accuracy Fuzzy (% correct)
	0 - 1	1 - 1.5	1.5 - 2	> 2			
0 - 1	19	7	11	3	40	47.50	65.00
1 - 1.5	17	10	3		30	33.33	100.00
1.5 - 2	25	63	77	9	174	44.25	85.63
> 2	1	15	131	196	343	57.14	95.34
Reference Total	62	95	222	208	587		
Producer's Accuracy Pure (% correct)	30.65	10.53	34.68	94.23	0.51448041		
Producer's Accuracy Fuzzy (% correct)	58.06	84.21	95.05	98.56	0.90630324		
Overall Classification Pure = 51.45%							
Overall Classification Fuzzy = 90.63%							

unsupervised classification was used to discriminate between vegetative cover and non-vegetative cover (i.e. vegetation vs cobble and water). This was followed by a supervised classification approach for the vegetative cover. To help discriminate among different vegetation types, homogeneous stands of the varying cover types (e.g., cottonwood, willow, reed canary grass, dry grass) were identified and associated with specific hyperspectral signatures. These specific imagery signatures were used as “training areas” to classify the image into the different land cover types. Mean spectral signatures (Figure 16) were calculated for each cover type and subsequently used in a supervised classification. Using the spectral signatures, the Mixed Tune Matched Filtering (MTMF) algorithm in ENVI (RSI 2000) was then applied to the vegetative component of the imagery to discriminate the varying vegetation types. For each reach, a final land cover map was produced consisting of 8 dominant cover types (i.e., water, cobble, deciduous – predominately cottonwood, willow, mixed grasses, dry grasses, reed canary grass, and shadows). In the Twin reach, willows were not easily differentiated from cottonwood; therefore, cottonwood and willow were aggregated into a single coverage identified as a “deciduous” category. A pasture category was also added in the Conant reach.

This method of classifying vegetation is a significant departure from approaches involving digitizing and photo-interpretation. We were able to take this approach of conducting an integrated supervised and unsupervised classification because of the application of the hyperspectral imagery allowing vegetation specific differentiation. We were also then able to conduct various analyses on the vegetation coverage that would not have been feasible using traditional photo-interpretation methods.

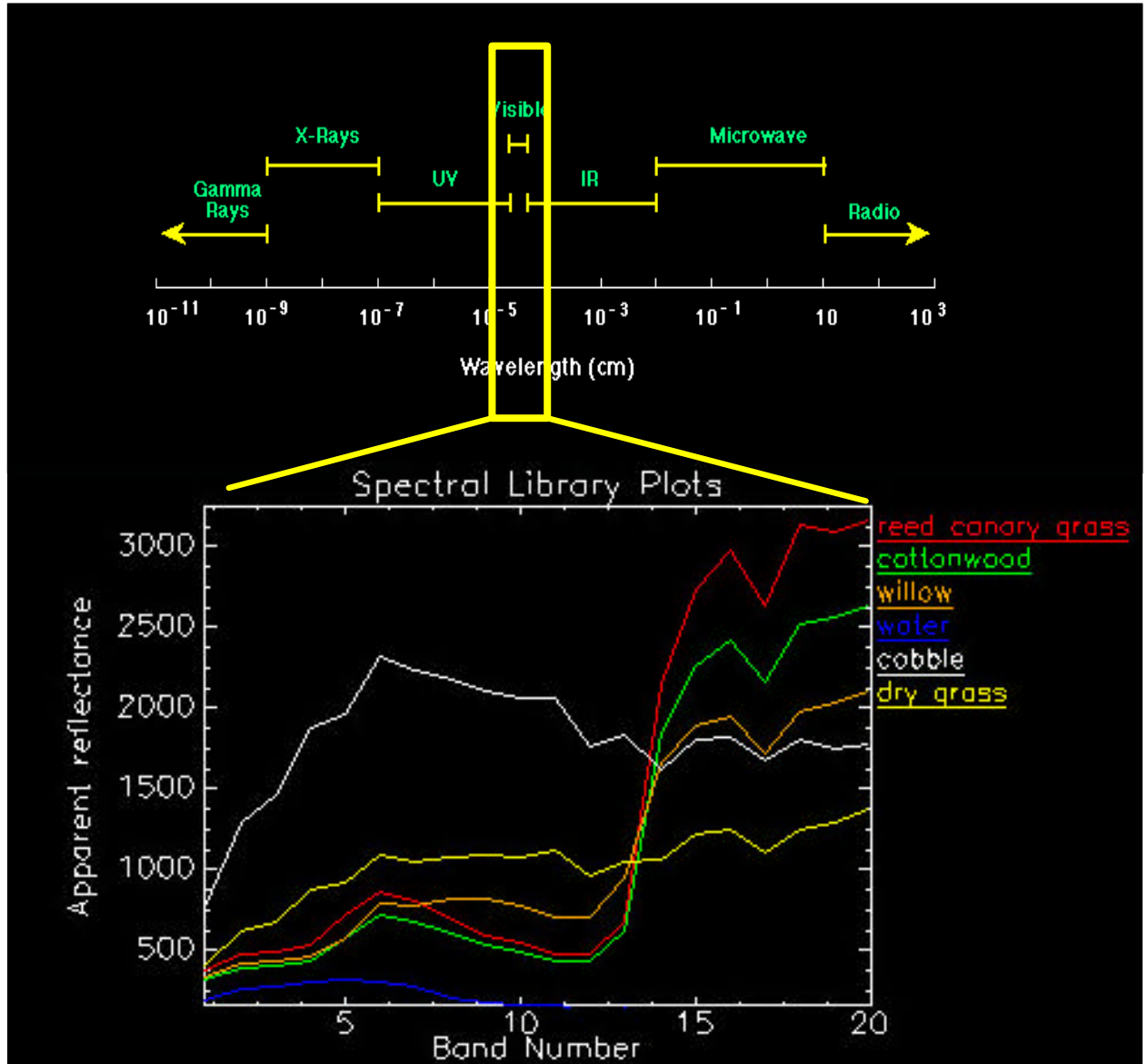


Figure 16. Mean spectral signatures of the hyperspectral reflectance data calculated for each cover type and subsequently used in a supervised classification.